

1                   **Introducing the MISR Level 2 Near Real-Time Aerosol Product**

2  
3  
4  
5  
6  
7  
8  
9  
10  
11  
12  
13  
14  
15  
16  
17  
18  
19  
20  
21  
22  
23  
24  
25  
26  
27  
28

Marcin. L. Witek<sup>1</sup>, Michael J. Garay<sup>1</sup>, David J. Diner<sup>1</sup>, Michael A. Bull<sup>1</sup>, Felix C. Seidel<sup>1</sup>, Abigail M. Nastan<sup>1</sup>, and Earl G. Hansen<sup>1</sup>

<sup>1</sup>Jet Propulsion Laboratory, California Institute of Technology, 4800 Oak Grove Drive, Pasadena, CA 91109, USA

**Abstract**

Atmospheric aerosols are an important element of Earth's climate system, and have significant impacts on the environment and on human health. Global aerosol modeling has been increasingly used for operational forecasting and as support to decision making. For example, aerosol analyses and forecasts are routinely used to provide air quality information and alerts in both civilian and military applications. The growing demand for operational aerosol forecasting calls for additional observational data that can be assimilated into models to improve model accuracy and predictive skill. These factors have motivated the development, testing, and release of a new near real-time (NRT) level 2 (L2) aerosol product from the Multi-angle Imaging SpectroRadiometer (MISR) instrument on NASA's Terra platform. The NRT product capitalizes on the unique attributes of the MISR aerosol retrieval approach and product contents, such as reliable aerosol optical depth as well as aerosol microphysical information. Several modifications are described that allow for rapid product generation within a three-hour window following acquisition of the satellite observations. Implications for the product quality and consistency are discussed as compared to the current operational L2 MISR aerosol product. Several ways of implementing additional use-specific retrieval screenings are also highlighted.

@ 2021. California Institute of Technology. Government sponsorship acknowledged

29 **1. Introduction**

30

31 Atmospheric aerosols have for long been recognized to influence the climate, environment, and  
32 human health (e.g., IPCC, 2013; Lelieveld et al., 2015; Shindell et al., 2013; Turnock et al.,  
33 2020). They also affect satellite remote sensing of important geophysical parameters such as  
34 ocean color (e.g., Frouin et al., 2019; Gordon, 1997) or greenhouse gas abundance (Butz et al.,  
35 2009; Frankenberg et al., 2012; Houweling et al., 2005). Aerosol particles and their properties  
36 have been extensively studied in-situ and remotely: from the ground, in the air, and from space.  
37 These observational data vary in spatial and temporal coverage, but usually only offer  
38 snapshots of local conditions. Since atmospheric aerosols have a life cycle ranging from hours  
39 to days, numerical modeling of their emission, transport, and deposition has filled the coverage  
40 gaps and extended our understanding of their global impacts. This has given rise to a number of  
41 global aerosol reanalyses (Gelaro et al., 2017; Inness et al., 2013, 2019; Lynch et al., 2016;  
42 Rienecker et al., 2011) that provide a long-range, gridded, and internally consistent outlook on  
43 aerosol burdens around the world. Furthermore, global aerosol modeling has been increasingly  
44 used for operational forecasting (e.g., Xian et al., 2019) and as support to decision making, for  
45 example in air quality alerts and in non-civilian applications (Liu et al., 2007).

46 The growing demand for consistent gridded aerosol products has been driving  
47 development and steady improvement of numerical predictions. [For example, the International  
48 Cooperation for Aerosol Prediction initiative was founded in 2010 \(Benedetti et al., 2011; Reid et  
49 al., 2011\), with one of its goals being the development of global multi-model aerosol forecasting  
50 ensemble for basic research and operational use \(Xian et al., 2019\).](#) Still, models suffer from  
51 often poorly resolved aerosol emissions and sinks and can be affected by errors in the  
52 underlying meteorology. As a result, systematic and sampling-related biases in aerosol fields  
53 are often found between model simulations and satellite observations (e.g., Buchard et al.,  
54 2015; Colarco et al., 2010; Lamarque et al., 2013; Zhang and Reid, 2009). An effective way to  
55 mitigate some of these problems is by assimilating aerosol observations into numerical models  
56 (e.g., Bocquet et al., 2015; Fu et al., 2017; Sekiyama et al., 2010; Di Tomaso et al., 2017;  
57 Werner et al., 2019; Zhang et al., 2008). Satellite observations of aerosol optical and  
58 microphysical properties are inseparable from these data assimilation activities as they offer the  
59 necessary data volume, near-global coverage, and frequent repeat cycle. However, an often-  
60 considerable latency for generating science-quality “standard” satellite products (8 to 40 hours)  
61 renders them unsuitable for operational forecasting. This has led to the development of aerosol

62 products within the time frame required by modeling centers, usually three hours from satellite  
63 overpass. A number of near real-time (NRT) products has emerged.

64 One example of a platform that provides users with NRT satellite products and imagery  
65 is NASA's Land, Atmosphere Near real-time Capability for EOS (LANCE) project  
66 (<https://earthdata.nasa.gov/earth-observation-data/near-real-time>). A range of instruments  
67 deliver various Level 1 (L1) and Level 2 (L2) data products  
68 ([https://earthdata.nasa.gov/collaborate/open-data-services-and-software/data-information-](https://earthdata.nasa.gov/collaborate/open-data-services-and-software/data-information-policy/data-levels)  
69 [policy/data-levels](https://earthdata.nasa.gov/collaborate/open-data-services-and-software/data-information-policy/data-levels)), including radiances, land surface properties, and atmospheric  
70 thermodynamics and composition within three hours from satellite observation. NRT aerosol  
71 products are currently available from the Moderate Resolution Imaging Spectroradiometer  
72 (MODIS), Ozone Monitoring Instrument (OMI), and Visible Infrared Imaging Radiometer Suite  
73 (VIIRS). NASA's Multi-angle Imaging SpectroRadiometer (MISR) currently provides NRT  
74 radiance and cloud motion vector products. The purpose of this paper is to introduce a new  
75 MISR NRT L2 aerosol product available within LANCE.

76 This paper is organized as follows. Section 2 and 3 provide brief descriptions of the  
77 MISR instrument and the data processing sequence, respectively. Section 4 first outlines the  
78 cloud identification methods employed in the MISR aerosol algorithm and then describes  
79 algorithmic modifications introduced in the NRT processing. Adjustments to cloud and retrieval  
80 screening parameters and their implications are discussed. The global distributions of the NRT  
81 product are analyzed in Section 5. Section 6 provides a summary.

82

## 83 **2. MISR instrument and aerosol data product**

84

85 The MISR instrument flies aboard the NASA Earth Observing System (EOS) Terra satellite,  
86 launched in December 1999 to a sun-synchronous descending polar orbit, at an orbital altitude  
87 of 705 km, an orbital period of 99 minutes, and an equatorial crossing time of 10:30 a.m. local  
88 time. MISR makes 14.56 orbits per day with a repetition cycle (revisit) of 16 days. The orbit  
89 tracks are georeferenced to a fixed set of 233 ground paths. With a cross-track swath of about  
90 380 km, total Earth coverage is obtained every 9 days at the equator and every 2 days at high  
91 latitudes.

92 MISR contains nine pushbroom cameras with viewing angles at the Earth's surface  
93 ranging from 0° (nadir) to +/- 70.5° oriented along the direction of the flight track. A point on the  
94 ground is imaged by all nine cameras in approximately 7 minutes. The cameras make  
95 observations of reflected solar radiance in four spectral bands, centered at 446 (blue), 558

Deleted: range

97 (green), 672 (red), and 866 (near-infrared) nm. The spatial resolution depends on the camera  
98 and wavelength. The red band has a full 275 m resolution in all cameras. The other three  
99 spectral channels are averaged onboard to a 1.1 km resolution in global-mode operation (Diner  
100 et al., 1998), with the exception of the nadir camera which preserves the full 275 m resolution in  
101 all spectral channels. See <https://misr.jpl.nasa.gov/Mission/> for more details.

102 MISR employs two processing pathways for aerosol retrievals, one for observations over  
103 land (Martonchik et al., 2009), and another for dark water (DW) (Kalashnikova et al., 2013),  
104 which applies over deep oceans, seas, and lakes. Previous versions of the MISR aerosol  
105 product were extensively validated over the years (e.g., Kahn et al., 2010; Kahn and Gaitley,  
106 2015; Kalashnikova et al., 2013; Shi et al., 2014; Witek et al., 2013) showing high retrieval  
107 quality over land and ocean.

108 The current operational version of the MISR aerosol product, designated as version 23  
109 (V23), was released publicly in June 2018. It introduced multiple algorithmic, data product, and  
110 data usability improvements (Garay et al., 2020; Witek et al., 2018a, 2018b). V23 provides  
111 aerosol information with a spatial resolution of 4.4 km x 4.4 km packaged in NetCDF-4 format.  
112 Initial validation efforts showed that V23 retrievals are more accurate than previous versions,  
113 with most pronounced improvements in the DW algorithm (Garay et al., 2020). V23 retrievals  
114 over oceans were extensively validated by Witek et al. (2019), indicating excellent agreement  
115 with ground-based observations. Other V23 Aerosol Optical Depth (AOD) evaluation efforts  
116 show similar results (e.g., Choi et al., 2019; Sayer et al., 2020; Si et al., 2020; Sogacheva et al.,  
117 2020). A first regional insight into retrieved particle properties from the MISR V23 aerosol  
118 product shows that MISR generally captures the distinct spatial and temporal features of aerosol  
119 type in East Asia (Tao et al., 2020). Furthermore, V23 has greatly improved the quality of  
120 reported AOD uncertainties, which now realistically represent retrieval errors (Sayer et al., 2020;  
121 Witek et al., 2019). This is especially relevant as pixel-level retrieval uncertainties are very  
122 important for satellite data assimilation, which is being increasingly used in aerosol modeling  
123 studies (Lynch et al., 2016; Shi et al., 2011, 2013; Zhang and Reid, 2010). MISR data and  
124 related documentation can be obtained from: <https://asdc.larc.nasa.gov/project/MISR>.

125

### 126 **3. NRT latency and data description**

127

128 MISR currently provides several L1 and L2 near real-time (NRT) radiance and cloud motion  
129 vector products ([https://earthdata.nasa.gov/earth-observation-data/near-real-time/download-nrt-](https://earthdata.nasa.gov/earth-observation-data/near-real-time/download-nrt-data/misr-nrt)  
130 [data/misr-nrt](https://earthdata.nasa.gov/earth-observation-data/near-real-time/download-nrt-data/misr-nrt)). All MISR NRT processing is based on Level 0 data downlinked in observational

131 sessions. These session-based files, representing portions of a single MISR orbit, usually cover  
132 between 10 to 50 minutes of observations, as compared to the full orbit period of 98.9 minutes.  
133 This session-based processing is necessary to allow for the fast product delivery required for  
134 NRT applications.

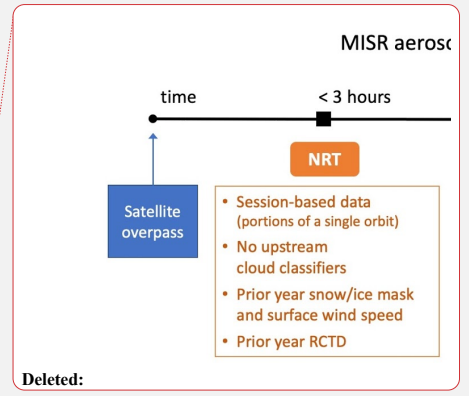
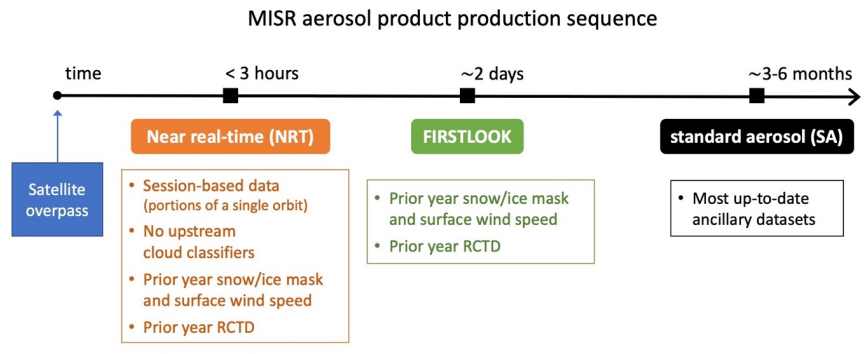
135 The new NRT L2 aerosol product file content, described in Data Product Specification  
136 ([https://asdc.larc.nasa.gov/documents/misr/DPS\\_AEROSOL\\_NRT\\_V023.20210430.pdf](https://asdc.larc.nasa.gov/documents/misr/DPS_AEROSOL_NRT_V023.20210430.pdf)), is  
137 equivalent to the standard aerosol product (Garay et al., 2020). The NRT L2 aerosol product file  
138 name convention is:

139 MISR\_AM1\_AS\_AEROSOL\_T{yyyymmddHHMMSS}\_P{ppp}\_O{oooooo}\_F13\_0023.nc, where  
140 'yyyy', 'mm', and 'dd' are the year, month, and day, and 'HH', 'MM' and 'SS' are the hour,  
141 minute, and seconds, respectively. Furthermore, {ppp} is the three-digit path identifier (between  
142 001 and 233) and {oooooo} is the six-digit orbit number. The NRT L2 aerosol product files are  
143 available for download within three hours of acquisition at NASA's Atmospheric Science Data  
144 Center (ASDC) (<https://asdc.larc.nasa.gov/project/MISR>).

145 For clarity, it is important to distinguish between the three different MISR L2 aerosol  
146 products: NRT, FIRSTLOOK, and standard aerosol (SA) products (see Figure 1). NRT is  
147 generated within a three-hour time interval after acquisition and uses the same ancillary inputs  
148 as FIRSTLOOK. These include the monthly gridded (1.0 degree) snow/ice mask and surface  
149 wind speed from the Terrestrial Atmospheric and Surface Climatology (TASC) database and the  
150 seasonal Radiometric Camera-by-camera Threshold Dataset (RCTD) (Diner et al., 1999a). Both  
151 NRT and FIRSTLOOK utilize TASC and RCTD datasets from the current month/season in the  
152 prior year. The FIRSTLOOK product is generated within two days from acquisition and includes  
153 cloud classification parameters obtained from the L1 and L2 cloud products. The SA product is  
154 available after final processing is performed on a seasonal basis and within three months past  
155 the end of the season, which results in a 3–6-month latency. The final processing utilizes the  
156 most recent snow/ice and wind speed data.

Deleted: (ref)

Deleted: standard aerosol



159  
 160 Figure 1 Schematic showing MISR aerosol product delivery timeline. Snow/ice mask and surface wind speed data are monthly  
 161 averages. RCTD stands for Radiometric Camera-by-camera Threshold Dataset. MISR final production (SA) is processed on a  
 162 seasonal cycle and is often delayed one to three months past the end of each season, which results in up to 6-month latency.  
 163

164 **4. Cloud screening in the NRT MISR aerosol product**

166 **4.1. Cloud identification**

168 Identification of cloudy pixels is a critical element of all satellite aerosol remote sensing  
 169 algorithms. MISR employs several cloud identification strategies which can be loosely split into  
 170 two groups: the first group relies on cloud classifiers previously generated with MISR Level 2  
 171 Cloud Detection and Classification algorithm (Diner et al., 1999b), and the second group  
 172 includes build-in tests that are internal to the aerosol retrieval algorithm (Diner et al., 2008).  
 173

174 **4.1.1. Upstream cloud classifiers**

176 The operational MISR aerosol algorithm relies on a range of external input datasets that are  
 177 either static—for example, a monthly wind speed climatology—or that need to be generated  
 178 prior to aerosol retrievals in upstream processing. A notable example of such external inputs to  
 179 the SA and FIRSTLOOK algorithms are cloud classification parameters obtained from the MISR  
 180 L2 cloud product. An important implication of this dependency is that aerosol processing needs  
 181 to wait for the cloud product to be generated, creating a time lag that is prohibitive for NRT  
 182 applications. Typically, the L2 cloud product is generated within about 18 hours of overpass,

Deleted:

Deleted: standard product

Deleted: cloud screening

Deleted: T

Deleted: standard

188 and the MISR L2 FIRSTLOOK aerosol processing is completed within about 2 days. In order to  
189 produce an L2 aerosol product within an about three-hour time frame, the algorithm needs to  
190 operate without the upstream cloud classifiers.

191 Two specific L2 cloud classification parameters utilized in [FIRSTLOOK and SA](#) aerosol  
192 processing are the MISR Stereoscopically-Derived Cloud Mask (SDCM) and the Angular  
193 Signature Cloud Mask (ASCM) (Diner et al., 1999b; Girolamo and Davies, 1994). In addition to  
194 these L2 products, the Radiometric Camera-by-camera Cloud Mask (RCCM) (Diner et al.,  
195 1999a; Girolamo and Davies, 1995) retrieved in L1B processing is also employed. All three  
196 parameters are reported at 1.1 km x 1.1 km resolution. It should be noted that RCCM also  
197 serves as an input to the algorithm that generates SDCM and ASCM, indicating that these  
198 parameters are not independent.

199 In the [FIRSTLOOK and SA](#) algorithm, the RCCM, SDCM, and ASCM cloud masks are  
200 used together to determine whether a particular 1.1 km x 1.1 km subregion is clear or cloudy.  
201 The implication is that if any of the 9 MISR cameras is designated as cloudy in a subregion, this  
202 subregion is excluded from aerosol retrieval. The clear/cloudy decision logic depends on the  
203 underlying surface type, assigned into three categories: land, water, and snow/ice. Generally, a  
204 “clear” outcome is favored over the two most frequently used surface types, land and water,  
205 assigning a subregion as cloudy only if the RCCM and SDCM masks indicate a cloud. The logic  
206 is considerably more conservative over snow/ice surfaces due to difficulties in distinguishing  
207 clouds from the underlying bright features. Details of the cloud mask decision logic over different  
208 surface types can be found in Diner et al. (2008).

209 Analyzing three months of V23 L2 [SA](#) product (March, April, May, 2020) indicates that  
210 the cloud masks along with the brightness test (see 4.1.2) lead to screening of about 50% of  
211 retrievals. As such, they have the largest impact on identifying and removing pixels where  
212 clouds might be present. These masks and decision pathways, however, have their deficiencies  
213 and additional checks were put in place to further decrease the frequency of cloud-  
214 contaminated aerosol retrievals.

215

#### 216 **4.1.2. Build-in cloud detection methods**

217

218 In addition to the cloud masks retrieved in the L1B processing (RCCM) and from the L2 Cloud  
219 Detection and Classification algorithm (SDCM, ASCM), the MISR aerosol retrieval algorithm  
220 relies on three internal tests to further identify cloudy pixels that might have escaped earlier  
221 detection. These are (1) the *brightness test*, (2) the *angle-to-angle smoothness test*, and (3) the

Deleted: standard aerosol

Deleted: aerosol

224 *angle-to-angle correlation test*. Details of these tests can be found in Diner et al. (2008) or Witek  
225 et al. (2013), but a short summary is provided here for completeness.

226 The brightness test is employed to identify clouds that lacked sufficient texture to be  
227 picked up by SDCM. For each surface type a fixed threshold is adopted on measured  
228 bidirectional reflectance factors (BRFs), and when exceeded in all spectral bands for at least  
229 one camera, it renders a subregion unsuitable for aerosol retrieval. The thresholds are set to  
230 1.0, 0.5, and 0.5 for snow/ice, land, and water surfaces, respectively. The value of 1.0 means  
231 that the brightness test is effectively turned off over snow/ice. Furthermore, the brightness test  
232 does not override subregions that were identified as clear by RCCM.

233 The angular smoothness test checks for unusually large variations in the measured  
234 equivalent reflectances as a function of camera angle, the premise being that in the absence of  
235 artifacts or subpixel clouds, the measured radiance should change smoothly from camera to  
236 camera. The test is achieved by fitting a polynomial to equivalent reflectances, separately for aft  
237 (+nadir) and forward (+nadir) cameras and each spectral band, and checking if the goodness of  
238 fit metric (definition in Diner et al., 2008) exceeds a threshold. If in at least one case the test  
239 fails, the subregion is eliminated.

240 Finally, the angle-to-angle correlation test also investigates radiance smoothness and  
241 correlation between camera angles, which makes it conceptually similar to the angular  
242 smoothness test, but instead utilizes high-resolution information from the red spectral band. It  
243 uses 4 x 4 arrays of the 275m spatial resolution red band equivalent reflectances in each 1.1 km  
244 x 1.1 km subregion. The test then evaluates spatial variability within the 4 x 4 array for each  
245 camera and compares it to a variability within a camera-average template. Variances,  
246 covariances, and normalized cross-correlations are calculated (see Diner et al., (2008) for  
247 details). If the variability within a camera deviates considerably from the average, this camera  
248 might have sub-pixel clouds or other contaminants, and as a result the subregion is excluded  
249 from aerosol retrievals.

250 In the three months of data analyzed in this study (March, April, May 2020), the relative  
251 occurrence of retrieval screening due the above-mentioned internal tests are about 4.0% and  
252 0.1% for the correlation and smoothness tests, respectively. These statistics come from  
253 analyzing the output field *Aerosol\_Retrieval\_Screening\_Flags* and as such they do not  
254 represent the absolute rates of success of each individual test. That is because the tests are  
255 performed in a sequential order and if one of them fails, tests that are next in sequence are not  
256 performed. For SA product generation, the order is: upstream cloud mask described in 4.1.1,  
257 the brightness test, the correlation test, and the smoothness test. For example, the correlation

Deleted: standard aerosol



259 test is only performed on pixels that already passed the upstream cloud tests as well as the  
260 brightness test. Additionally, the brightness test does not have its own flag in the  
261 *Aerosol\_Retrieval\_Screening\_Flags* output but is grouped together with the upstream cloud  
262 classifiers.

263

#### 264 **4.2. Retrieval screening using regional cloud parameters**

265

266 Methods described in section 4.1 focus on identifying and excluding cloudy 1.1 km x 1.1 km  
267 subregions from the aerosol retrieval process. The retrieval region consists of 16 (4 x 4)  
268 subregions. These methods are highly effective at removing cloud-contaminated pixels, but  
269 since they rely on MISR visible wavelengths they might miss certain cloud signatures more  
270 easily detected in the infrared spectrum (e.g., Gao et al., 1993). For example, MODIS routinely  
271 uses its reflective and emissive infrared channels to detect optically thin cirrus clouds  
272 (Ackerman et al., 2010; Levy et al., 2013). As a result, MISR cloud detection methods  
273 occasionally fail, which leads to visible outliers in retrieved AODs (Witek et al., 2018b). For that  
274 reason, an additional set of screenings is applied in an effort to eliminate such unusually high  
275 AOD retrievals (Garay et al., 2020). Two of these additional methods look at overall cloudiness  
276 in the retrieval region (consisting of 4 x 4 subregions) as well as in a larger area consisting of 3  
277 x 3 regions (12 x 12 subregions). The Cloud Screening Parameter (CSP) represents the fraction  
278 of clear grid cells within a region, whereas Cloud Screening Parameter Neighbor 3x3 (CSP9) is  
279 similar to CSP but for the larger area. If CSP is below 0.7 and CSP9 below 0.5, the retrieval is  
280 not reported in the final product intended for most users. However, it is still included in the  
281 product's AUXILIARY subcategory and annotated with the term "Raw" to indicate that the  
282 product has not undergone recommended quality screenings.

283

#### 284 **4.3. Adjusting cloud screening thresholds**

285

##### 286 **4.3.1. Performance of the prototype NRT product**

287

288 This subsection presents results and analysis of prototype NRT aerosol retrievals. These are  
289 obtained prior to any threshold and screening adjustments included in the final version of the  
290 product. To differentiate between the final and the prototype NRT products, the latter is denoted  
291 as  $NRT_{\text{prot}}$ .

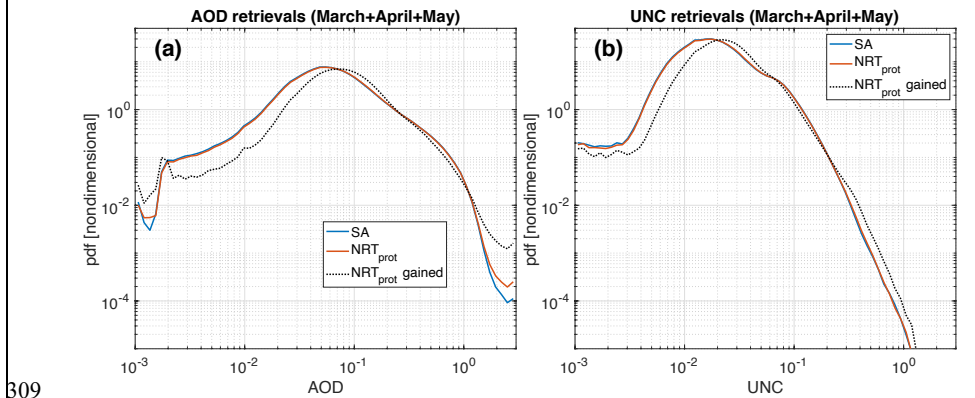
292 As mentioned in the previous section, the NRT processing cannot rely on the cloud  
 293 masks generated in the L1 and L2 cloud products, namely the RCCM, SDCM, and ASCM. This  
 294 implies that potentially less screening of cloudy subregions would be applied, increasing the  
 295 probability of cloud contamination in aerosol retrievals. However, some of the burden of cloud  
 296 identification is picked up by the built-in cloud tests described in section 4.1.2. The frequency of  
 297 these tests identifying cloudy pixels increases in NRT processing in comparison to standard  
 298 processing, in large part mitigating the negative consequences resulting from the lack of the  
 299 upstream cloud masks. This is well evidenced by examining the normalized probability density  
 300 functions (*pdfs*) of AOD from spring 2020 (Figure 2). The SA (red) and NRT<sub>prot</sub> (blue) lines are  
 301 very similar, indicating that the built-in cloud tests substitute to a significant extent for the  
 302 missing upstream cloud masks in generating the NRT<sub>prot</sub> product. The largest difference occurs  
 303 in the high-AOD range, suggesting that NRT<sub>prot</sub> has more retrievals in this regime. The black  
 304 dotted line shows a *pdf* of the NRT<sub>prot</sub> AOD retrievals that do not have a matching SA retrieval.  
 305 This is labeled as “NRT<sub>prot</sub> gained” as it represents additional retrievals obtained in NRT  
 306 processing due to the lack of external cloud masks. The “NRT<sub>prot</sub> gained” *pdf* is clearly shifted  
 307 towards higher AODs, confirming that the NRT<sub>prot</sub> processing tends to retrieve higher AODs in  
 308 places where SA is not available.

Deleted: FIRSTLOOK

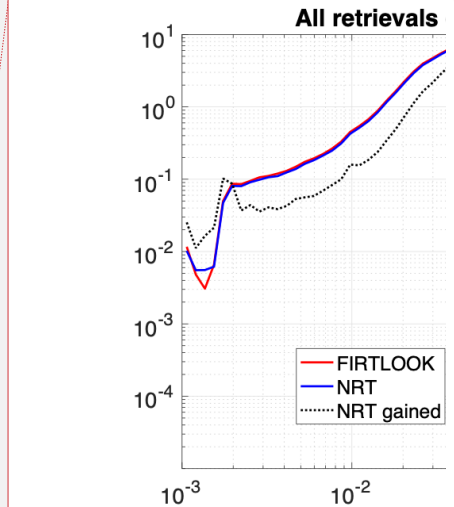
Deleted: FIRSTLOOK

Formatted: Subscript

Deleted: FIRSTLOOK



309 Figure 2 (a) AOD normalized probability density functions from SA, prototype NRT, and prototype NRT retrievals that do not  
 310 have a matching SA equivalent (labeled as NRT<sub>prot</sub> gained); (b) same as in (a) but for retrieved AOD uncertainties (UNC). Data  
 311 statistics for AODs are provided in Table 1.



Deleted:

Deleted: FIRSTLOOK

Deleted: FIRSTLOOK

Deleted: .

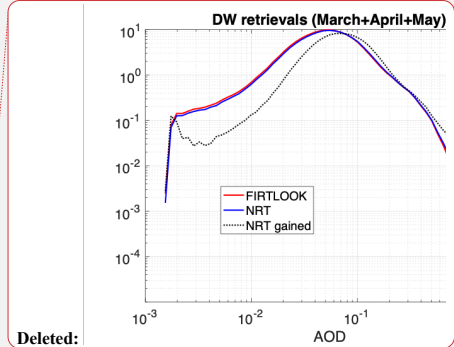
313 Figure 3 shows *pdfs* of AOD but with retrievals separated between DW (Fig. 3a) and  
 314 land (Fig. 3b). These *pdfs* indicate that the retrievals over oceans are the main source of

322 increased frequency of high-AODs in the NRT<sub>prot</sub> product. The pdfs over land are virtually  
 323 unchanged, including a slightly flattened but still relatively comparable distribution of the "NRT<sub>prot</sub>  
 324 gained" retrievals (Fig. 3b). The additional statistics of the data presented in Figs. 2 and 3,  
 325 including the retrieval count, the mean AOD, and the geometric mean AOD, which is better  
 326 suited for log-normal distributions of AOD (Sayer and Knobelspiesse, 2019), are provided in  
 327 Table 1. Note that the number of NRT<sub>prot</sub> gained is not the same as the number of NRT<sub>prot</sub> minus  
 328 SA. This is because some SA retrievals do not have their NRT<sub>prot</sub> equivalent, making the SA  
 329 count larger than it would have been otherwise.  
 330 In the 3-month period analyzed in this study (March, April, May, 2020), the NRT<sub>prot</sub>  
 331 processing leads to about 6.4% more retrievals than SA (see Table 1). 5.5 million NRT<sub>prot</sub>  
 332 retrievals do not have a matching SA retrieval (NRT gained), and the majority of them (67%) are  
 333 DW retrievals. The overall geometric means are almost identical in SA and NRT<sub>prot</sub>, although  
 334 small variations in this statistic are seen in DW and land categories. The NRT gained have  
 335 visibly higher mean and geometric mean values, the increase coming mainly from DW  
 336 retrievals. These basic statistics warrant a further look at the NRT<sub>prot</sub> performance over DW.

Deleted: similar ...istribution of the "NRT<sub>prot</sub> gained" retrievals (Fig. 3b). The additional statistics of the data presented in Figs. 2 and 3, including the retrieval count, the mean AOD, and the geometric mean AOD, which is better suited for log-normal distributions of AOD (Sayer and Knobelspiesse, 2019)(Sayer et al. 2020) ... [1]

Formatted ... [2]

Deleted:  
 Deleted: 5... more retrievals than SA FIRSTLOOK (see Table 1). 5.54...million NRT<sub>prot</sub> retrievals do not have a matching SA/FIRSTLOOK ...retrieval (NRT gained), and the majority of them (678...) are DW retrievals. The overall geometric means are almost identical in SA FIRSTLOOK ... [3]



Deleted:  
 Deleted: Same as in Fig. 2 but with retrievals ...or land (a) and DW (b) retrievals, respectively. separated between DW (a) and land (b). ... [4]

Formatted: Subscript

Formatted: Subscript

Formatted: Subscript

Deleted: FL

Formatted: Subscript

Deleted: FL

Formatted: Subscript

Deleted: FL

Formatted: Subscript

Deleted: 50...7.4 ... [5]

Deleted: 53.7

Deleted: 5.4

Deleted: 27.9

Deleted: 31.1

Deleted: 22.5

Deleted: 22.6

Deleted: 1.7

337  
 338 Figure 3 AOD pdfs for land (a) and DW (b) retrievals, respectively. Data statistics are provided in Table 1.

	All retrievals			DW			Land	
	SA	NRT <sub>prot</sub>	NRT <sub>prot</sub> gained	SA	NRT <sub>prot</sub>	NRT <sub>prot</sub> gained	SA	NRT <sub>prot</sub>
N (×10 <sup>6</sup> )	49.7	52.9	5.5	27.6	30.7	3.7	22.1	22.2

mean	0.168	0.169	0.171	0.111	0.115	0.146	0.240	0.243
geomean	0.111	0.112	0.122	0.083	0.085	0.106	0.160	0.162

Table 1 Additional statistics for the data presented in Figs. 2 and 3 (statistic for FIRSTLOOK not shown). NRT gained stands for the prototype NRT retrievals that do not have a matching SA equivalent; geomean stands for the geometric mean AOD.

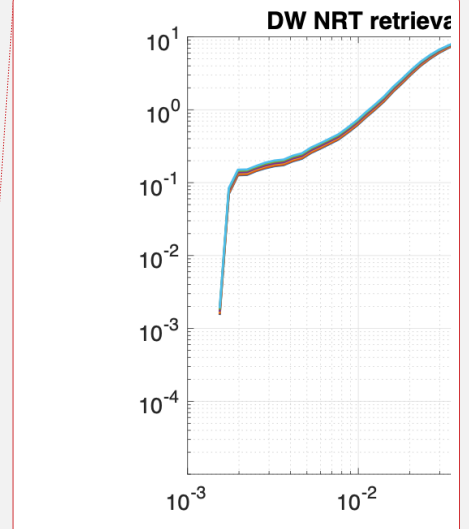
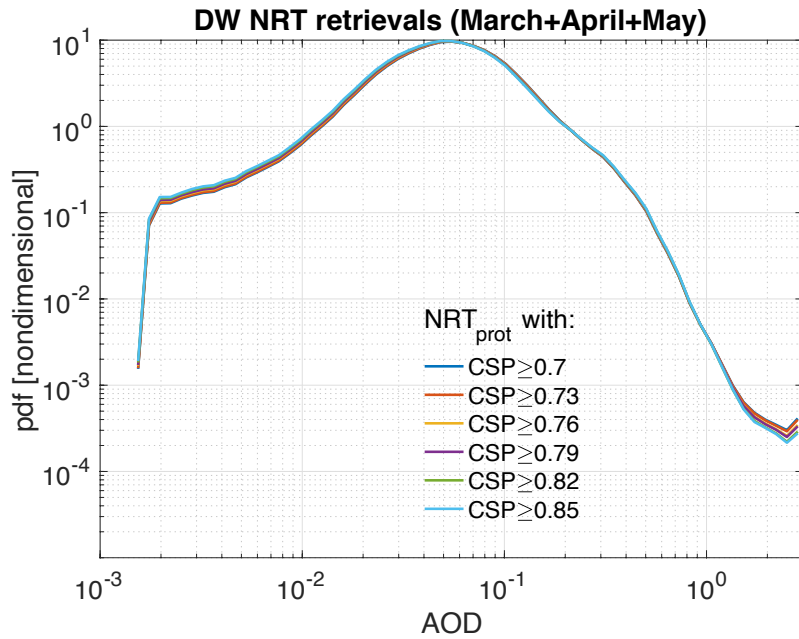
### 4.3.2. Sensitivity to CSP and CSP9 thresholds in DW retrievals

One way to screen potentially cloud-contaminated high-AOD retrievals is to adjust thresholds on CSP and CSP9 parameters (Garay et al., 2020). This is furthermore justified by the fact that in the absence of RCCM, SDCM, and ASCM in NRT<sub>prot</sub> processing, fewer cloudy subregions are identified in a retrieval area and consequently CSP and CSP9 have by default lower values. This argument provides strong justification for investigating sensitivity to increased CSP and CSP9 thresholds in the NRT<sub>prot</sub> processing.

The SA product uses the thresholds of CSP=0.7 and CSP9=0.5 (Garay et al., 2020); when the values of CSP and CSP9 are below these thresholds in a retrieval region, the aerosol retrieval is removed from the data field recommended for users. Figure 4 and Table 2 show pdfs and AOD statistics for different thresholds of CSP and CSP9 parameters in the NRT<sub>prot</sub> product over dark water surfaces. There are only minor changes in the pdfs when the thresholds are increased, including in the high-AOD regime. The mean and geometric mean decrease gradually but slowly; even at the highest considered thresholds (0.85 for CSP and 0.75 for CSP9) these statistics are still above the SA values. At the same time the number of passing NRT<sub>prot</sub> retrievals decreases considerably faster, with almost 19% of retrievals lost when the highest thresholds are used. These results indicate that adjusting CSP and CSP9 thresholds is not an effective strategy to constraining NRT<sub>prot</sub> retrievals.

- Deleted: 0.167
- Deleted: 0.167
- Deleted: 0.172
- Deleted: 0.110
- Deleted: 0.237
- Deleted: 0.240
- Deleted: 0.228
- Deleted: 0.110
- Deleted: 0.111
- Deleted: 0.121
- Deleted: 0.082
- Deleted: 0.157
- Deleted: 0.159
- Deleted: FL stand for FIRSTLOOK;
- Deleted: FIRSTLOOK
- Deleted: less
- Deleted: standard

- Deleted: FIRSTLOOK
- Deleted: over



- Deleted:
- Deleted: 31.1
- Deleted: 30.5
- Deleted: 28.8
- Deleted: 28.1
- Deleted: 26.2
- Deleted: 25.1
- Deleted: FIRSTLOOK
- Deleted: 1.7
- Deleted: 7.3
- Deleted: 9.7
- Deleted: 19.2
- Deleted: 27.9
- Deleted: 0.1147
- Deleted: 0.1145
- Deleted: 0.1141
- Deleted: 0.114
- Deleted: 0.1138
- Deleted: 0.1139
- Deleted: 0.1105
- Formatted ... [6]
- Deleted: 0.0848
- Deleted: 0.0846
- Deleted: 0.0840
- Deleted: 0.0837
- Deleted: 0.0832
- Deleted: 0.0830
- Deleted: 0.0824

432  
433  
434

Figure 4 Prototype NRT AOD pdfs over dark water surfaces from spring 2020 obtained with different CSP and CSP9 cloud-screening thresholds. Data statistics are provided in Table 2.

N ( $\times 10^6$ )	30.7	30.1 (-1.9%)	28.4 (-7.4%)	27.7 (-9.8%)	25.9 (-15.6%)	24.9 (-18.9%)	SA 27.6
CSP	$\geq 0.7$	$\geq 0.73$	$\geq 0.76$	$\geq 0.79$	$\geq 0.82$	$\geq 0.85$	
CSP9	$\geq 0.5$	$\geq 0.55$	$\geq 0.6$	$\geq 0.65$	$\geq 0.7$	$\geq 0.75$	
mean	0.1151 ± 0.1200	0.1149 ± 0.1199	0.1145 ± 0.1190	0.1144 ± 0.1191	0.1142 ± 0.1185	0.1143 ± 0.1189	0.1110 ± 0.1079
geomean	0.0850	0.0847	0.0841	0.0839	0.0834	0.0832	0.0826

Table 2 Additional statistics for the data presented in Fig. 4. Values for CSP and CSP9 indicate their corresponding thresholds for screening AOD retrievals. The arithmetic mean values are accompanied by their respective  $\pm$  one standard deviations.

435  
436  
437  
438

4.3.3. Sensitivity to ARCI threshold in DW retrievals

493

494 V23 of the MISR aerosol product introduced a new parameter, called the aerosol retrieval  
495 confidence index (ARCI), that is used to screen high-AOD retrieval outliers caused by cloud  
496 contamination and other factors (Witek et al., 2018b). ARCI, defined only for DW retrievals,  
497 proved to be an efficient metric at filtering out potentially cloud-contaminated AOD retrievals. In  
498 standard processing, retrievals with  $ARCI < 0.15$  are removed from the recommended user  
499 field, but are retained in the AUXILIARY group. The 0.15 threshold is well supported through  
500 statistical analysis (Witek et al., 2018b), although some erroneous AODs still pass this  
501 screening method, suggesting that increasing this threshold might be beneficial in NRT  
502 processing.

503 Figure 5 and Table 3 show *pdfs* and AOD statistics for different thresholds of ARCI in the  
504 NRT<sub>prot</sub> product. In this case the differences between ARCI thresholds are quite noticeable,  
505 especially in the high-AOD range of retrievals. Increasing the ARCI threshold to 0.2 leads to a  
506 loss of about 11% of NRT<sub>prot</sub> DW retrievals, but the resulting mean and geometric mean are  
507 lower than the *SA* values. At the same time, the absolute number of NRT<sub>prot</sub> DW retrievals (27.4  
508 million) is still comparable to the number of *SA* DW retrievals (27.6 million). The *pdfs* and the  
509 statistics suggest that increasing the NRT<sub>prot</sub> ARCI threshold from 0.15 to 0.18 leads to a  
510 product that has similar characteristics to *SA*.

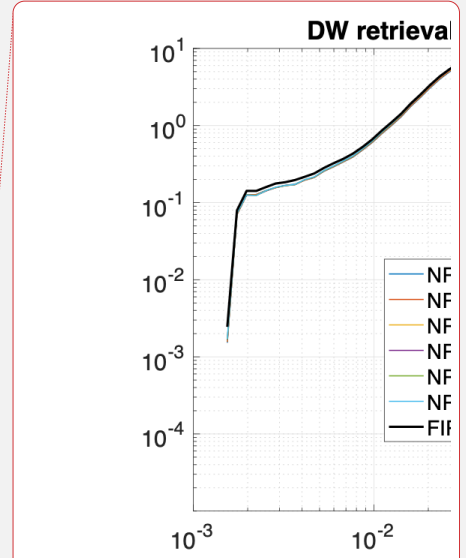
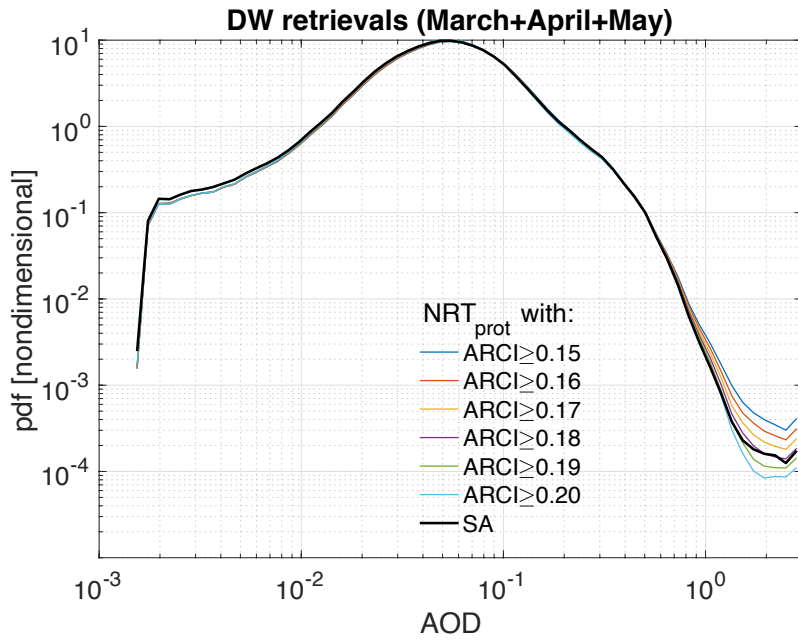
Deleted: FIRSTLOOK

Deleted: 8

Deleted: FIRSTLOOK

Deleted: 9

Deleted: FIRSTLOOK



Deleted:

Deleted: 31.1

Deleted: 30.4

Deleted: 29.8

Deleted: 29.1

Deleted: 28.4

Deleted: 27.8

Deleted: Firstlook

Deleted: 8.7

Deleted: 27.9

Deleted: 1147

Deleted: 1133

Deleted: 1120

Deleted: 1108

Deleted: 1096

Deleted: 1086

Deleted: 11...110 ± 0.107905

... [7]

Deleted: 0849

Deleted: 0841

Deleted: 0834

Deleted: 0826

Deleted: 0819

Deleted: 0812

Deleted: 0824

516  
517  
518

Figure 5 Prototype NRT AOD pdfs from spring 2020 obtained with different ARCI thresholds. Data statistic are provided in Table 3.

N	30.7	30.0	29.4	28.7	28.0	27.4	SA
( $\times 10^6$ )		(-2.2%)	(-4.3%)	(-6.5%)	(-8.6%)	(-10.8%)	27.6
ARCI	$\geq 0.15$	$\geq 0.16$	$\geq 0.17$	$\geq 0.18$	$\geq 0.19$	$\geq 0.20$	
mean	0.1151 ± 0.1200	0.1137 ± 0.1157	0.1124 ± 0.1122	0.1112 ± 0.1094	0.1100 ± 0.1070	0.1090 ± 0.1051	0.1110 ± 0.1079
geomean	0.0850	0.0842	0.0835	0.0828	0.0821	0.0813	0.0826

Table 3 Additional statistic for the data presented in Fig. 5.

519  
520  
521  
522

#### 4.3.4. Recommendation for NRT processing

572 The statistical analyses presented in the previous sections indicate that the lack of RCCM,  
573 SDCM, and ASCM in NRT processing has negative consequences on the product, especially by  
574 allowing more, potentially cloud-contaminated, high-AOD DW retrievals to pass screening  
575 criteria. Adjusting build-in cloud screening thresholds on CSP and CSP9 brings only limited  
576 benefits at the cost of losing a considerable percentage of retrievals. However, the ARCI  
577 threshold adjustments result in much closer statistical correspondence between the  $NRT_{prot}$  and  
578 standard AOD retrievals. For that reason, a revised ARCI threshold of 0.18 is implemented in  
579 NRT processing. Since the unscreened retrievals, as well as the ARCI parameter, are also  
580 provided in the AUXILIARY group of the product, users are encouraged to experiment with their  
581 own thresholds which might prove more beneficial in specific applications or geographic areas.  
582

Deleted: FIRSTLOOK

#### 583 4.4. Cloud/clear decision logic over snow/ice

584  
585 In section 4.1.1 the impact of upstream cloud classifiers in standard processing—namely the  
586 RCCM, SDCM, and ASCM—on the subregion’s cloud/clear designation was briefly described.  
587 The decision pathway depends on the underlying surface type, which can be either land, water,  
588 or snow/ice. Over land and water, the “cloud” outcome is only obtained when both RCCM and  
589 SDCM designate the subregion as cloudy. In the absence of RCCM and SDCM the default  
590 outcome is “clear”. Over snow/ice, however, the logic is more restrictive and favors the “cloudy”  
591 designation (Diner et al., 2008). Specifically, when the upstream cloud classifiers are not  
592 available, the subregion designation is set to “cloudy” by default. This has important implications  
593 on aerosol retrievals in areas where snow and ice occur seasonally.

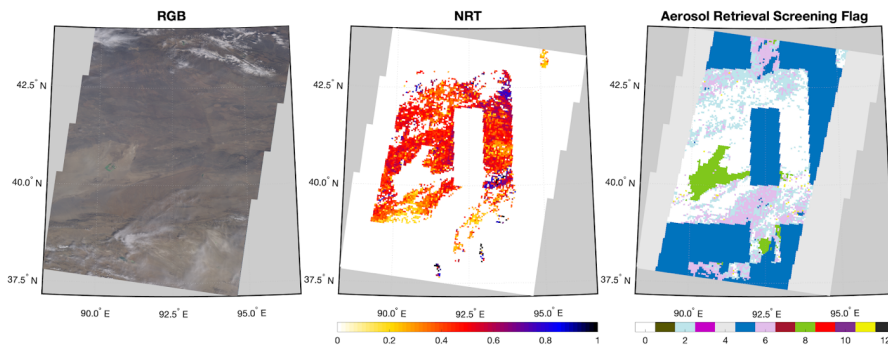
594 The snow/ice surface mask, unlike land and water, is not static and changes every  
595 month. Furthermore, the snow/ice mask input to MISR aerosol processing has a 1.0-degree  
596 horizontal resolution, which is re-gridded to a 1.1 km resolution corresponding to the resolution  
597 of MISR subregion. In FIRSTLOOK processing, the snow/ice mask from the same month but in  
598 the previous year is used. The final SA processing is performed when the current year’s monthly  
599 snow/ice mask becomes available. The NRT processing, similarly to FIRSTLOOK, relies on the  
600 previous year’s snow/ice mask. Additionally, given the lack of upstream cloud classifiers, the  
601 snow/ice areas are designated as “cloudy” for aerosol retrieval purposes. This is well visualized  
602 in Figure 6 which shows the visible image and the corresponding maps of AOD and Aerosol  
603 Retrieval Screening Flag in the NRT processing. The dark blue color (index 5) denotes cloudy  
604 regions determined using the snow/ice cloud logic. The box-like nature of the excluded areas is  
605 associated with the coarse resolution of the snow/ice mask (1.0 degree). The previous year’s

Deleted: standard

Deleted: FIRSTLOOK retrievals use



609 mask might also not be representative of the current conditions on the ground. It is worth noting  
 610 that the FIRSTLOOK product often suffers from the same exclusion rules as NRT. This is  
 611 because of the strict clear/cloud logic over snow/ice surfaces which favors the cloudy outcome;  
 612 in the case shown in Fig. 6 the AOD gaps in FIRSTLOOK (not shown) look very similar to the  
 613 NRT product.



614  
 615 *Figure 6 Example of snow/ice masking in NRT AOD retrievals. (Left) Visible image of the retrieval area. (Center) Corresponding*  
 616 *NRT AOD retrievals. (Right) NRT Aerosol Retrieval Screening Flag for the same area; the dark blue color denotes regions*  
 617 *designated as cloudy.*

618 Several attempts have been made by the MISR science team to improve NRT aerosol  
 619 retrievals in snow/ice covered areas. However, identifying and isolating snow-covered surfaces  
 620 in the absence of upstream cloud classifiers proves very challenging. The quality of aerosol  
 621 retrievals is often negatively affected in such conditions. For that reason, and in an attempt to  
 622 eliminate as many NRT AOD outliers as possible, the current snow/ice logic is retained in the  
 623 NRT aerosol processing.

624

625 **5. NRT and SA differences**

626

627 In this section, geographic distributions of MISR AOD retrievals from SA and NRT products are  
 628 analyzed. The datasets encompass three months, March, April, and May of 2020. The NRT  
 629 AOD retrievals are screened with the revised ARCI threshold of 0.18 as suggested in section  
 630 4.3.4. The spatial overlap of the SA and NRT data is achieved using an intersect of the X\_Dim  
 631 and Y\_Dim fields in the two data products.

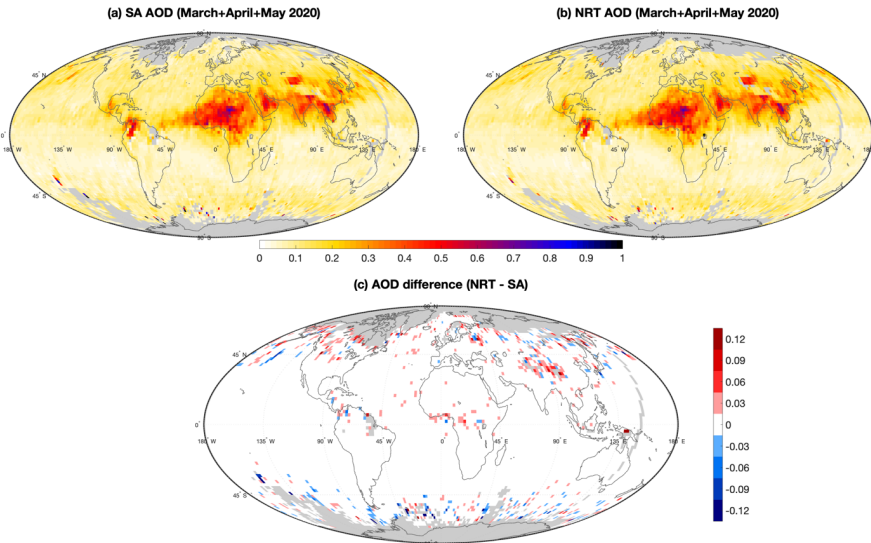
Deleted: FIRSTLOOK

Deleted: FIRSTLOOK

Deleted: FIRSTLOOK

635 Figure 7 shows the global distributions of geometric mean AOD from the (a) SA and (b)  
 636 NRT products. The retrievals are gridded at 2-by-2-degree spatial resolution. Fig. 7c shows the  
 637 AOD difference between the two products (NRT - SA).

638 The largest AOD differences are seen in areas with climatologically high cloud cover,  
 639 especially over the Southern Ocean, and over land in areas where potential snow cover could  
 640 be an issue. Over the Southern Ocean, the SA AODs are predominantly higher than the NRT  
 641 AODs. This is due to the increased ARCI threshold in NRT (0.18 vs. 0.15 in SA) which brings in  
 642 more aggressive screening of cloud-contaminated retrievals (Witek et al., 2018b). Over land,  
 643 where the ARCI parameter is not available, the gridded NRT AODs tend to be higher than the  
 644 SA AODs, which is in part related to the differences in snow/ice mask between the two  
 645 products. Still, the AOD differences in Fig. 7c are rather small and reflect sampling issues rather  
 646 than any systematic deficiencies in NRT processing. At the same time the lack of cloud  
 647 classifiers in NRT does not adversely affect AOD distributions, which is consistent with the  
 648 statistical analysis presented in section 4.2.3.



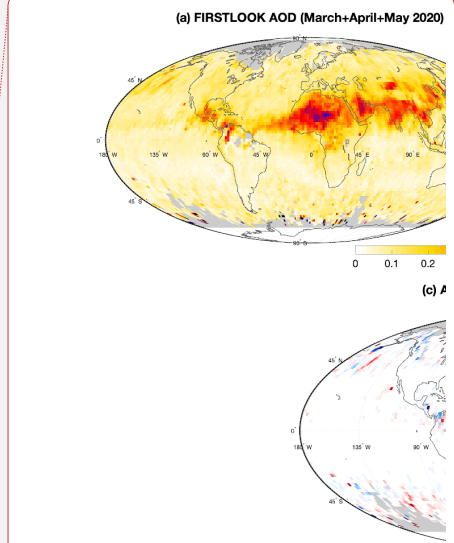
649  
 650 Figure 7 (a) Global distribution of SA AOD geometric mean values across March, April, and May of 2020 on a 2-by-2-degree  
 651 spatial resolution; (b) same as in (a) but for NRT AOD; and (c) AOD difference between SA and NRT. Grid points with less  
 652 than 15 retrievals are excluded.

Deleted: FIRSTLOOK

Deleted: In those regions

Deleted: FIRSTLOOK

Deleted: FIRSTLOOK

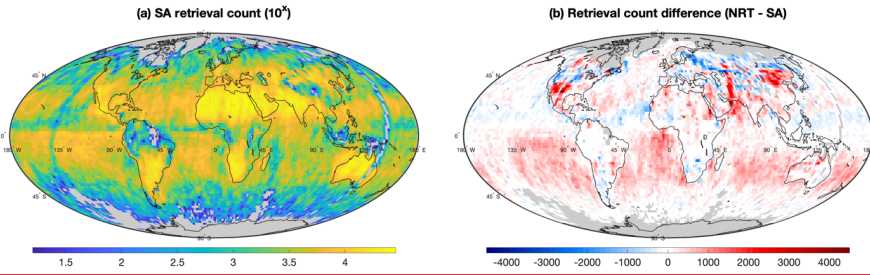


Deleted:

Deleted: FIRSTLOOK

Deleted: FIRSTLOOK

660 Figure 8 complements Fig. 7 by showing (a) the SA retrieval count distribution as well as  
 661 (b) the retrieval count difference between the SA and NRT products.



662  
 663 Figure 8 (a) Decimal logarithm of the retrieval count from the SA product in March, April, and May of 2020; (b) retrieval count  
 664 difference between SA and NRT. Presented values are gridded at 2-by-2-degree spatial resolution and grid points with less than  
 665 15 retrievals are excluded.

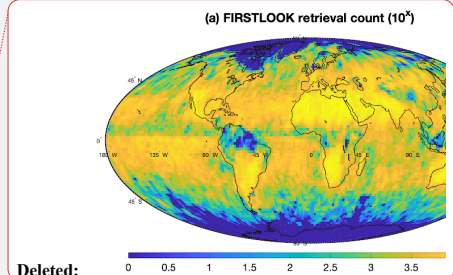
666 The highest number of retrievals is found over the subtropical continents where the  
 667 cloud cover is usually the smallest. Over the subtropical oceans in the Southern Hemisphere the  
 668 NRT retrieval counts are typically higher than in SA, which results from the absence of upstream  
 669 cloud classifiers in NRT processing and subsequently fewer subregions being excluded as  
 670 cloudy. Note that this increase in retrieval count caused by the lack of cloud classifiers is not  
 671 compensated by the increased ARCI threshold in NRT processing ( $ARCI \geq 0.18$ ), which always  
 672 reduces the number of retrievals when compared to the default SA threshold ( $ARCI \geq 0.15$ ). The  
 673 lack of hemispheric symmetry in this case is likely due to the seasonal variability (only months in  
 674 northern spring are analyzed here). Over land the lack of upstream cloud classifiers also results  
 675 in higher number of NRT retrievals in certain regions, but the surface type exclusion rules  
 676 reverse this pattern, especially at higher latitudes. The conservative cloud logic over snow/ice  
 677 surfaces in NRT processing often results in the lower number of NRT retrievals in the high  
 678 latitudes of the northern hemisphere.

679  
 680 **6. Summary**  
 681

682 The MISR V23 aerosol product, publicly available since mid-2018, is a high-resolution state-of-  
 683 the-art data product from NASA's Terra flagship mission. V23 AOD retrievals have remarkable  
 684 accuracy compared against ground-based observations (Garay et al., 2020; Tao et al., 2020;  
 685 Witek et al., 2019) and the product is more intuitive and easier to use than previous versions.

Deleted: FIRSTLOOK

Deleted: FIRSTLOOK



Deleted:

Deleted: FIRSTLOOK

Deleted: FIRSTLOOK

Deleted: lower

Deleted: FIRSTLOOK

Deleted: is attributed to

Deleted: DW retrievals

695 The product is available within 2 days from satellite overpass as a FIRSTLOOK version, and  
696 within 3-to-6 months as a final science-quality SA version that employs the most up-to-date  
697 ancillary datasets. In response to the needs of operational user communities, a new MISR L2  
698 NRT aerosol product has been developed with a 3-hour latency.

Deleted: "standard"

699 The new NRT algorithm does not depend on the upstream cloud classifiers that are  
700 generated in L1 and L2 cloud processing. The lack of cloud classifiers is in large part mitigated  
701 by the aerosol algorithm's built-in cloud identification methods. Analysis of the prototype NRT  
702 product has shown an increased frequency of high-AOD retrievals, especially over oceans and  
703 in climatologically cloudy areas, likely due to an increase in cloud contamination. Adjusting the  
704 ARCI threshold in DW retrievals proves highly effective at eliminating some of these high-AOD  
705 outliers and improves the NRT product's statistical agreement with the SA version. The new  
706 NRT aerosol product applies an ARCI threshold of 0.18 to mitigate cloud contamination in the  
707 absence of upstream cloud masks in NRT processing. The remaining differences in statistical  
708 and geographic distributions between the NRT and SA AODs, which includes information from  
709 the L2 cloud product, are small and largely confined to areas with high cloud cover.

Deleted: FIRSTLOOK

Deleted: FIRSTLOOK

710 The results of this study also serve as an example of the effects of screening threshold  
711 adjustments in MISR aerosol retrievals on AOD statistics and distributions. Researchers  
712 interested in particular applications and/or specific geographic regions are encouraged to  
713 experiment with their own threshold to achieve most optimal results. The NRT aerosol product  
714 contains both the recommended product contained within the main science directory  
715 "4.4 KM PRODUCTS" that has the stricter ARCI threshold (ARCI $\geq$ 0.18), and the unscreened  
716 product without the additional cloud and ARCI filtering designed for more experienced users,  
717 located within the AUXILIARY group.

## 719 Acknowledgements

720 This research was carried out at the Jet Propulsion Laboratory, California Institute of  
721 Technology, under a contract with the National Aeronautics and Space Administration. Support  
722 from the MISR project is acknowledged. Special thanks to Andrew Sayer and one anonymous  
723 reviewer for carefully reading the manuscript and providing valuable comments.

## 725 Data availability

726 The MISR V23 SA and NRT data is publicly available and can be downloaded from  
727 <https://10dup05.larc.nasa.gov/cgi-bin/MISR/main.cgi>. MISR NRT data is not stored permanently

Formatted: Font: Bold

731 and is only available for three to six months from the time of acquisition; please contact the  
732 corresponding author to request the NRT data from the months analyzed in this study.

733

734

**Deleted:** All data analyzed in this study are publicly available, although the transient nature of FIRSTLOOK and NRT products might limit their availability. The data can be downloaded from <https://0dup05.larc.nasa.gov/cgi-bin/MISR/main.cgi>.

740 **References:**

- 741 Ackerman, S., Richard, F., Kathleen, S., Yinghui, L., Liam, G., Bryan, B. and Paul, M.:  
742 Discriminating clear-sky from cloud with MODIS algorithm theoretical basis document  
743 (MOD35), Univ. Wisconsin - Madison, 6th Edn.(October), 129 [online] Available from:  
744 <http://citeseerx.ist.psu.edu/viewdoc/summary?doi=10.1.1.385.4885>, 2010.
- 745 Benedetti, A., Reid, J. S. and Colarco, P. R.: International cooperative for aerosol prediction  
746 workshop on aerosol forecast verification, in *Bulletin of the American Meteorological Society*,  
747 vol. 92., 2011.
- 748 Bocquet, M., Elbern, H., Eskes, H., Hirtl, M., Aabkar, R., Carmichael, G. R., Flemming, J.,  
749 Inness, A., Pagowski, M., Pérez Camaño, J. L., Saide, P. E., San Jose, R., Sofiev, M., Vira, J.,  
750 Baklanov, A., Carnevale, C., Grell, G. and Seigneur, C.: Data assimilation in atmospheric  
751 chemistry models: Current status and future prospects for coupled chemistry meteorology  
752 models, *Atmos. Chem. Phys.*, 15(10), 5325–5358, doi:10.5194/acp-15-5325-2015, 2015.
- 753 Buchard, V., Da Silva, A. M., Colarco, P. R., Darmenov, A., Randles, C. A., Govindaraju, R.,  
754 Torres, O., Campbell, J. and Spurr, R.: Using the OMI aerosol index and absorption aerosol  
755 optical depth to evaluate the NASA MERRA Aerosol Reanalysis, *Atmos. Chem. Phys.*, 15(10),  
756 5743–5760, doi:10.5194/acp-15-5743-2015, 2015.
- 757 Butz, A., Hasekamp, O. P., Frankenberg, C. and Aben, U.: Retrievals of atmospheric CO<sub>2</sub> from  
758 simulated space-borne measurements of backscattered near-infrared sunlight: Accounting for  
759 aerosol effects, *Appl. Opt.*, 48, 3322–3336, doi:10.1364/AO.48.003322, 2009.
- 760 Choi, M., Lim, H., Kim, J., Lee, S., Eck, T. F., Holben, B. N., Garay, M. J., Hyer, E. J., Saide, P.  
761 E. and Liu, H.: Validation, comparison, and integration of GOCI, AHI, MODIS, MISR, and  
762 VIIRS aerosol optical depth over East Asia during the 2016 KORUS-AQ campaign, *Atmos.*  
763 *Meas. Tech.*, 12(8), 4619–4641, doi:10.5194/amt-12-4619-2019, 2019.
- 764 Colarco, P., Da Silva, A., Chin, M. and Diehl, T.: Online simulations of global aerosol  
765 distributions in the NASA GEOS-4 model and comparisons to satellite and ground-based aerosol  
766 optical depth, *J. Geophys. Res. Atmos.*, 115(14), doi:10.1029/2009JD012820, 2010.

767 Diner, D. J., Beckert, J. C., Reilly, T. H., Bruegge, C. J., Conel, J. E., Kahn, R. A., Martonchik,  
768 J. V., Ackerman, T. P., Davies, R., Gerstl, S. A. W., Gordon, H. R., Muller, J. P., Myneni, R. B.,  
769 Sellers, P. J., Pinty, B. and Verstraete, M. M.: Multiangle Image Spectroradiometer (MISR)  
770 instrument description and experiment overview, *IEEE Trans. Geosci. Remote Sens.*, 36(4),  
771 1072–1087, 1998.

772 Diner, D. J., Di Girolamo, L. and Clothiaux, E. E.: Level 1 Cloud Detection Algorithm  
773 Theoretical Basis, *Jet Propuls. Lab. Calif. Inst. Technol.*, D-13397(Rev. B), 1999a.

774 Diner, D. J., Davies, R., Di Girolamo, L., Horvath, A., Moroney, C., Muller, J. P., Paradise, S.  
775 R., Wenkert, D. and Zong, J.: Level 2 Cloud Detection and Classification Algorithm Theoretical  
776 Basis, *Jet Propuls. Lab. Calif. Inst. Technol.*, D-11399(Rev. D), 1999b.

777 Diner, D. J., Abdou, W. A., Ackerman, T. P., Crean, K., Gordon, H. R., Kahn, R. A.,  
778 Martonchik, J. V., McMuldroy, S., Paradise, S. R. and Pinty, B.: Level 2 aerosol retrieval  
779 algorithm theoretical basis, *Jet Propuls. Lab. Calif. Inst. Technol.*, D-11400(Rev. G), 2008.

780 Frankenberg, C., Hasekamp, O., O’Dell, C., Sanghavi, S., Butz, A. and Worden, J.: Aerosol  
781 information content analysis of multi-angle high spectral resolution measurements and its benefit  
782 for high accuracy greenhouse gas retrievals, *Atmos. Meas. Tech.*, 5(7), 1809–1821,  
783 doi:10.5194/amt-5-1809-2012, 2012.

784 Frouin, R. J., Franz, B. A., Ibrahim, A., Knobelspiesse, K., Ahmad, Z., Cairns, B., Chowdhary,  
785 J., Dierssen, H. M., Tan, J., Dubovik, O., Huang, X., Davis, A. B., Kalashnikova, O., Thompson,  
786 D. R., Remer, L. A., Boss, E., Coddington, O., Deschamps, P. Y., Gao, B. C., Gross, L.,  
787 Hasekamp, O., Omar, A., Pelletier, B., Ramon, D., Steinmetz, F. and Zhai, P. W.: Atmospheric  
788 Correction of Satellite Ocean-Color Imagery During the PACE Era, *Front. Earth Sci.*, 7,  
789 doi:10.3389/feart.2019.00145, 2019.

790 Fu, G., Prata, F., Xiang Lin, H., Heemink, A., Segers, A. and Lu, S.: Data assimilation for  
791 volcanic ash plumes using a satellite observational operator: A case study on the 2010  
792 Eyjafjallajökull volcanic eruption, *Atmos. Chem. Phys.*, 17(2), 1187–1205, doi:10.5194/acp-17-  
793 1187-2017, 2017.

794 Gao, B. C., Goetz, A. F. H. and Wiscombe, W. J.: Cirrus cloud detection from Airborne Imaging  
795 Spectrometer data using the 1.38  $\mu\text{m}$  water vapor band, *Geophys. Res. Lett.*, 20(3), 301–304,  
796 doi:10.1029/93GL00106, 1993.

797 Garay, M. J., Witek, M. L., Kahn, R. A., Seidel, F. C., Limbacher, J. A., Bull, M. A., Diner, D.  
798 J., Hansen, E. G. E. G., Kalashnikova, O. V., Lee, H., Nastan, A. M. and Yu, Y.: Introducing the  
799 4.4km spatial resolution Multi-Angle Imaging SpectroRadiometer (MISR) aerosol product,  
800 *Atmos. Meas. Tech.*, 13(2), 593–628, doi:10.5194/amt-13-593-2020, 2020.

801 Gelaro, R., McCarty, W., Suárez, M. J., Todling, R., Molod, A., Takacs, L., Randles, C. A.,  
802 Darmenov, A., Bosilovich, M. G., Reichle, R., Wargan, K., Coy, L., Cullather, R., Draper, C.,  
803 Akella, S., Buchard, V., Conaty, A., da Silva, A. M., Gu, W., Kim, G. K., Koster, R., Lucchesi,  
804 R., Merkova, D., Nielsen, J. E., Partyka, G., Pawson, S., Putman, W., Rienecker, M., Schubert,  
805 S. D., Sienkiewicz, M. and Zhao, B.: The modern-era retrospective analysis for research and  
806 applications, version 2 (MERRA-2), *J. Clim.*, 30(14), 5419–5454, doi:10.1175/JCLI-D-16-  
807 0758.1, 2017.

808 Girolamo, L. Di and Davies, R.: A Band-Differenced Angular Signature Technique for Cirrus  
809 Cloud Detection, *IEEE Trans. Geosci. Remote Sens.*, 32(4), 890–896, doi:10.1109/36.298017,  
810 1994.

811 Girolamo, L. Di and Davies, R.: The Image Navigation Cloud Mask for the Multiangle Imaging  
812 Spectroradiometer (MISR), *J. Atmos. Ocean. Technol.*, 12(6), doi:10.1175/1520-  
813 0426(1995)012<1215:tinmf>2.0.co;2, 1995.

814 Gordon, R.: Atmospheric correction of ocean color imagery in the Earth Observing System era,  
815 *J. Geophys. Res. - Atmos.*, 102(D14), 17081–17106, doi:10.1029/96JD02443, 1997.

816 Houweling, S., Hartmann, W., Aben, I., Schrijver, H., Skidmore, J., Roelofs, G. J. and Breon, F.  
817 M.: Evidence of systematic errors in SCIAMACHY-observed CO<sub>2</sub> due to aerosols, *Atmos.*  
818 *Chem. Phys.*, 5(11), 3003–3013, doi:10.5194/acp-5-3003-2005, 2005.

819 Inness, A., Baier, F., Benedetti, A., Bouarar, I., Chabrillat, S., Clark, H., Clerbaux, C., Coheur,  
820 P., Engelen, R. J., Errera, Q., Flemming, J., George, M., Granier, C., Hadji-Lazaro, J., Huijnen,



821 V., Hurtmans, D., Jones, L., Kaiser, J. W., Kapsomenakis, J., Lefever, K., Leitão, J., Razinger,  
822 M., Richter, A., Schultz, M. G., Simmons, A. J., Suttie, M., Stein, O., Thépaut, J. N., Thouret,  
823 V., Vrekoussis, M. and Zerefos, C.: The MACC reanalysis: An 8 yr data set of atmospheric  
824 composition, *Atmos. Chem. Phys.*, 13(8), 4073–4109, doi:10.5194/acp-13-4073-2013, 2013.

825 Inness, A., Ades, M., Agustí-Panareda, A., Barré, J., Benedictow, A., Blechschmidt, A.-M.,  
826 Dominguez, J. J., Engelen, R., Eskes, H., Flemming, J., Huijnen, V., Jones, L., Kipling, Z.,  
827 Massart, S., Parrington, M., Peuch, V.-H., Razinger, M., Remy, S., Schulz, M. and Suttie, M.:  
828 The CAMS reanalysis of atmospheric composition, *Atmos. Chem. Phys.*, 19(6), 3515–3556,  
829 doi:10.5194/acp-19-3515-2019, 2019.

830 IPCC: Climate Change 2013: The Physical Science Basis. Contribution of Working Group I to  
831 the Fifth Assessment Report of the Intergovernmental Panel on Climate Change, edited by T. F.  
832 Stocker, D. Qin, G. K. Plattner, M. M. B. Tignor, S. K. Allen, J. Boschung, A. Nauels, Y. Xia,  
833 V. Bex, and P. M. Midgley, Cambridge University Press, Cambridge, United Kingdom and New  
834 York, NY, USA., 2013.

835 Kahn, R. A. and Gaitley, B. J.: An analysis of global aerosol type as retrieved by MISR, J.  
836 *Geophys. Res. Atmos.*, 120(9), 4248–4281, doi:10.1002/2015JD023322, 2015.

837 Kahn, R. A., Gaitley, B. J., Garay, M. J., Diner, D. J., Eck, T. F., Smirnov, A. and Holben, B. N.:  
838 Multiangle Imaging SpectroRadiometer global aerosol product assessment by comparison with  
839 the Aerosol Robotic Network, *J. Geophys. Res. Atmos.*, 115(23), doi:10.1029/2010JD014601,  
840 2010.

841 Kalashnikova, O. V., Garay, M. J., Martonchik, J. V. and Diner, D. J.: MISR Dark Water aerosol  
842 retrievals: Operational algorithm sensitivity to particle non-sphericity, *Atmos. Meas. Tech.*, 6(8),  
843 2131–2154, doi:10.5194/amt-6-2131-2013, 2013.

844 Lamarque, J. F., Shindell, D. T., Josse, B., Young, P. J., Cionni, I., Eyring, V., Bergmann, D.,  
845 Cameron-Smith, P., Collins, W. J., Doherty, R., Dalsoren, S., Faluvegi, G., Folberth, G., Ghan,  
846 S. J., Horowitz, L. W., Lee, Y. H., MacKenzie, I. A., Nagashima, T., Naik, V., Plummer, D.,  
847 Righi, M., Rumbold, S. T., Schulz, M., Skeie, R. B., Stevenson, D. S., Strode, S., Sudo, K.,  
848 Szopa, S., Voulgarakis, A. and Zeng, G.: The atmospheric chemistry and climate model

849 intercomparison Project (ACCMIP): Overview and description of models, simulations and  
850 climate diagnostics, *Geosci. Model Dev.*, 6(1), 179–206, doi:10.5194/gmd-6-179-2013, 2013.

851 Lelieveld, J., Evans, J. S., Fnais, M., Giannadaki, D. and Pozzer, A.: The contribution of outdoor  
852 air pollution sources to premature mortality on a global scale, *Nature*, 525(7569), 367–371,  
853 doi:10.1038/nature15371, 2015.

854 Levy, R. C., Mattoo, S., Munchak, L. A., Remer, L. A., Sayer, A. M., Patadia, F. and Hsu, N. C.:  
855 The Collection 6 MODIS aerosol products over land and ocean, *Atmos. Meas. Tech.*, 6(11),  
856 2989–3034, doi:10.5194/amt-6-2989-2013, 2013.

857 Liu, M., Westphal, D. L., Walker, A. L., Holt, T. R., Richardson, K. A. and Miller, S. D.:  
858 COAMPS real-time dust storm forecasting during operation Iraqi freedom, *Weather Forecast.*,  
859 22(1), 192–206, doi:10.1175/WAF971.1, 2007.

860 Lynch, P., Reid, J. S., Westphal, D. L., Zhang, J., Hogan, T. F., Hyer, E. J., Curtis, C. A., Hegg,  
861 D. A., Shi, Y., Campbell, J. R., Rubin, J. I., Sessions, W. R., Turk, F. J. and Walker, A. L.: An  
862 11-year global gridded aerosol optical thickness reanalysis (v1.0) for atmospheric and climate  
863 sciences, *Geosci. Model Dev.*, 9(4), 1489–1522, doi:10.5194/gmd-9-1489-2016, 2016.

864 Martonchik, J. V., Kahn, R. A. and Diner, D. J.: Retrieval of aerosol properties over land using  
865 MISR observations, in *Satellite Aerosol Remote Sensing over Land*, pp. 267–293, Springer  
866 Berlin Heidelberg., 2009.

867 Reid, J. S., Benedetti, A., Colarco, P. R. and Hansen, J. A.: International operational aerosol  
868 observability workshop, in *Bulletin of the American Meteorological Society*, vol. 92., 2011.

869 Rienecker, M. M., Suarez, M. J., Gelaro, R., Todling, R., Bacmeister, J., Liu, E., Bosilovich, M.  
870 G., Schubert, S. D., Takacs, L., Kim, G. K., Bloom, S., Chen, J., Collins, D., Conaty, A., Da  
871 Silva, A., Gu, W., Joiner, J., Koster, R. D., Lucchesi, R., Molod, A., Owens, T., Pawson, S.,  
872 Pegion, P., Redder, C. R., Reichle, R., Robertson, F. R., Ruddick, A. G., Sienkiewicz, M. and  
873 Woollen, J.: MERRA: NASA’s modern-era retrospective analysis for research and applications,  
874 *J. Clim.*, 24, 3624–3648, doi:10.1175/JCLI-D-11-00015.1, 2011.

875 Sayer, A. M. and Knobelspiesse, K. D.: How should we aggregate data? Methods accounting for

876 the numerical distributions, with an assessment of aerosol optical depth, *Atmos. Chem. Phys.*,  
877 19(23), 15023–15048, doi:10.5194/acp-19-15023-2019, 2019.

878 Sayer, A. M., Govaerts, Y., Kolmonen, P., Lipponen, A., Luffarelli, M., Mielonen, T., Patadia,  
879 F., Popp, T., Povey, A. C., Stebel, K. and Witek, M. L.: A review and framework for the  
880 evaluation of pixel-level uncertainty estimates in satellite aerosol remote sensing, *Atmos. Meas.*  
881 *Tech.*, 13(2), 373–404, doi:10.5194/amt-13-373-2020, 2020.

882 Sekiyama, T. T., Tanaka, T. Y., Shimizu, A. and Miyoshi, T.: Data assimilation of CALIPSO  
883 aerosol observations, *Atmos. Chem. Phys.*, 10(1), 39–49, doi:10.5194/acp-10-39-2010, 2010.

884 Shi, Y., Zhang, J., Reid, J. S., Holben, B., Hyer, E. J. and Curtis, C.: An analysis of the collection  
885 5 MODIS over-ocean aerosol optical depth product for its implication in aerosol assimilation,  
886 *Atmos. Chem. Phys.*, 11(2), 557–565, doi:10.5194/acp-11-557-2011, 2011.

887 Shi, Y., Zhang, J., Reid, J. S., Hyer, E. J. and Hsu, N. C.: Critical evaluation of the MODIS Deep  
888 Blue aerosol optical depth product for data assimilation over North Africa, *Atmos. Meas. Tech.*,  
889 6(4), 949–969, doi:10.5194/amt-6-949-2013, 2013.

890 Shi, Y., Zhang, J., Reid, J. S., Liu, B. and Hyer, E. J.: Critical evaluation of cloud contamination  
891 in the MISR aerosol products using MODIS cloud mask products, *Atmos. Meas. Tech.*, 7(6),  
892 1791–1801, doi:10.5194/amt-7-1791-2014, 2014.

893 Shindell, D. T., Lamarque, J. F., Schulz, M., Flanner, M., Jiao, C., Chin, M., Young, P. J., Lee,  
894 Y. H., Rotstayn, L., Mahowald, N., Milly, G., Faluvegi, G., Balkanski, Y., Collins, W. J.,  
895 Conley, A. J., Dalsoren, S., Easter, R., Ghan, S., Horowitz, L., Liu, X., Myhre, G., Nagashima,  
896 T., Naik, V., Rumbold, S. T., Skeie, R., Sudo, K., Szopa, S., Takemura, T., Voulgarakis, A.,  
897 Yoon, J. H. and Lo, F.: Radiative forcing in the ACCMIP historical and future climate  
898 simulations, *Atmos. Chem. Phys.*, 13(6), 2939–2974, doi:10.5194/acp-13-2939-2013, 2013.

899 Si, Y., Chen, L., Xiong, X., Shi, S., Husi, L. and Cai, K.: Evaluation of the MISR fine resolution  
900 aerosol product using MODIS, MISR, and ground observations over China, *Atmos. Environ.*,  
901 223(December 2019), 117229, doi:10.1016/j.atmosenv.2019.117229, 2020.

902 Sogacheva, L., Popp, T., Sayer, A. M., Dubovik, O., Garay, M. J., Heckel, A., Hsu, N. C.,

903 Jethva, H., Kahn, R. A., Kolmonen, P., Kosmale, M., de Leeuw, G., Levy, R. C., Litvinov, P.,  
904 Lyapustin, A., North, P., Torres, O. and Arola, A.: Merging regional and global aerosol optical  
905 depth records from major available satellite products, *Atmos. Chem. Phys.*, 20(4), 2031–2056,  
906 doi:10.5194/acp-20-2031-2020, 2020.

907 Tao, M., Wang, J., Li, R., Chen, L., Xu, X., Wang, L., Tao, J., Wang, Z. and Xiang, J.:  
908 Characterization of Aerosol Type Over East Asia by 4.4 km MISR Product: First Insight and  
909 General Performance, *J. Geophys. Res. Atmos.*, 125(13), 1–16, doi:10.1029/2019JD031909,  
910 2020.

911 Di Tomaso, E., Schutgens, N. A. J., Jorba, O. and García-Pando, C. P.: Assimilation of MODIS  
912 Dark Target and Deep Blue observations in the dust aerosol component of NMMB-MONARCH  
913 version 1.0, *Geosci. Model Dev.*, 10(3), 1107–1129, doi:10.5194/gmd-10-1107-2017, 2017.

914 Turnock, S. T., Allen, R. J., Andrews, M., Bauer, S. E., Deushi, M., Emmons, L., Good, P.,  
915 Horowitz, L., John, J. G., Michou, M., Nabat, P., Naik, V., Neubauer, D., O’Connor, F. M.,  
916 O’livié, D., Oshima, N., Schulz, M., Sellar, A., Shim, S., Takemura, T., Tilmes, S., Tsigaridis, K.,  
917 Wu, T. and Zhang, J.: Historical and future changes in air pollutants from CMIP6 models,  
918 *Atmos. Chem. Phys.*, 20(23), 14547–14579, doi:10.5194/acp-20-14547-2020, 2020.

919 Werner, M., Kryza, M. and Guzikowski, J.: Can data assimilation of surface PM<sub>2.5</sub> and Satellite  
920 AOD improve WRF-Chem Forecasting? A case study for two scenarios of particulate air  
921 pollution episodes in Poland, *Remote Sens.*, 11(20), doi:10.3390/rs11202364, 2019.

922 Witek, M. L., Garay, M. J., Diner, D. J. and Smirnov, A.: Aerosol optical depths over oceans: A  
923 view from MISR retrievals and collocated MAN and AERONET in situ observations, *J.*  
924 *Geophys. Res. Atmos.*, 118(22), 12620–12633, doi:10.1002/2013JD020393, 2013.

925 Witek, M. L., Diner, D. J., Garay, M. J., Xu, F., Bull, M. A. and Seidel, F. C.: Improving MISR  
926 AOD Retrievals with Low-Light-Level Corrections for Veiling Light, *IEEE Trans. Geosci.*  
927 *Remote Sens.*, 56(3), 1251–1268, doi:10.1109/TGRS.2017.2727342, 2018a.

928 Witek, M. L., Garay, M. J., Diner, D. J., Bull, M. A. and Seidel, F. C.: New approach to the  
929 retrieval of AOD and its uncertainty from MISR observations over dark water, *Atmos. Meas.*

930 Tech., 11(1), 429–439, doi:10.5194/amt-11-429-2018, 2018b.

931 Witek, M. L., Garay, M. J., Diner, D. J. and Smirnov, A.: Oceanic Aerosol Loading Derived  
932 From MISR's 4.4 km (V23) Aerosol Product, *J. Geophys. Res. Atmos.*, 124(17–18), 10154–  
933 10174, doi:10.1029/2019JD031065, 2019.

934 Xian, P., Reid, J. S., Hyer, E. J., Sampson, C. R., Rubin, J. I., Ades, M., Asencio, N., Basart, S.,  
935 Benedetti, A., Bhattacharjee, P. S., Brooks, M. E., Colarco, P. R., da Silva, A. M., Eck, T. F.,  
936 Guth, J., Jorba, O., Kouznetsov, R., Kipling, Z., Sofiev, M., Perez Garcia-Pando, C., Pradhan,  
937 Y., Tanaka, T., Wang, J., Westphal, D. L., Yumimoto, K. and Zhang, J.: Current state of the  
938 global operational aerosol multi-model ensemble: An update from the International Cooperative  
939 for Aerosol Prediction (ICAP), *Q. J. R. Meteorol. Soc.*, 145, 176–209, doi:10.1002/qj.3497,  
940 2019.

941 Zhang, J. and Reid, J. S.: An analysis of clear sky and contextual biases using an operational  
942 over ocean MODIS aerosol product, *Geophys. Res. Lett.*, 36(15), doi:10.1029/2009GL038723,  
943 2009.

944 Zhang, J. and Reid, J. S.: A decadal regional and global trend analysis of the aerosol optical  
945 depth using a data-assimilation grade over-water MODIS and Level 2 MISR aerosol products,  
946 *Atmos. Chem. Phys.*, 10(22), 10949–10963, doi:10.5194/acp-10-10949-2010, 2010.

947 Zhang, J., Reid, J. S., Westphal, D. L., Baker, N. L. and Hyer, E. J.: A system for operational  
948 aerosol optical depth data assimilation over global oceans, *J. Geophys. Res. Atmos.*, 113(10), 1–  
949 13, doi:10.1029/2007JD009065, 2008.

950

Page 11: [1] Deleted Microsoft Office User 4/22/21 4:25:00 PM

Page 11: [1] Deleted Microsoft Office User 4/22/21 4:25:00 PM

Page 11: [2] Formatted Microsoft Office User 4/19/21 4:51:00 PM

Subscript

Page 11: [2] Formatted Microsoft Office User 4/19/21 4:51:00 PM

Subscript

Page 11: [2] Formatted Microsoft Office User 4/19/21 4:51:00 PM

Subscript

Page 11: [3] Deleted Microsoft Office User 4/19/21 4:00:00 PM

Page 11: [3] Deleted Microsoft Office User 4/19/21 4:00:00 PM

Page 11: [3] Deleted Microsoft Office User 4/19/21 4:00:00 PM

Page 11: [3] Deleted Microsoft Office User 4/19/21 4:00:00 PM

Page 11: [3] Deleted Microsoft Office User 4/19/21 4:00:00 PM

Page 11: [3] Deleted Microsoft Office User 4/19/21 4:00:00 PM

Page 11: [4] Deleted Microsoft Office User 4/22/21 3:30:00 PM

Page 11: [4] Deleted Microsoft Office User 4/22/21 3:30:00 PM

Page 11: [5] Deleted Microsoft Office User 4/19/21 12:18:00 PM

Page 11: [5] Deleted Microsoft Office User 4/19/21 12:18:00 PM

**Page 13: [6] Formatted    Microsoft Office User    4/22/21 10:13:00 AM**

Font: 9 pt

**Page 13: [6] Formatted    Microsoft Office User    4/22/21 10:13:00 AM**

Font: 9 pt

**Page 15: [7] Deleted    Microsoft Office User    4/19/21 12:42:00 PM**



**Page 15: [7] Deleted    Microsoft Office User    4/19/21 12:42:00 PM**

